Delft University of Technology

Document Version
Final published version

Licence
CC BY

Citation (APA)
Yan, L., van der Vleuten, R. F., Hagh, S. N., Jones, S., Aghajanloo, M., Schellart, M. A. R., Boersma, D., Voskov, D., & Farajzadeh, R. (2026). Exploring reservoir heterogeneity effects on halite precipitation during CO2 storage: insights from an experimental study. *Energy Conversion and Management: X*, *31*, Article 102070. https://doi.org/10.1016/j.ecmx.2026.102070

Important note
To cite this publication, please use the final published version (if applicable).
Please check the document version above.

Copyright
In case the licence states “Dutch Copyright Act (Article 25fa)”, this publication was made available Green Open Access via the TU Delft Institutional Repository pursuant to Dutch Copyright Act (Article 25fa, the Taverne amendment). This provision does not affect copyright ownership.
Unless copyright is transferred by contract or statute, it remains with the copyright holder.

Sharing and reuse
Other than for strictly personal use, it is not permitted to download, forward or distribute the text or part of it, without the consent of the author(s) and/or copyright holder(s), unless the work is under an open content license such as Creative Commons.

Takedown policy
Please contact us and provide details if you believe this document breaches copyrights.
We will remove access to the work immediately and investigate your claim.

This work is downloaded from Delft University of Technology.

Energy Conversion and Management: X 31 (2026) 102070

Contents lists available at ScienceDirect

Energy Conversion and Management: X

journal homepage: www.sciencedirect.com/journal/energy-conversion-and-management-x

Exploring reservoir heterogeneity effects on halite precipitation during CO_2 storage: insights from an experimental study

Lifei Yan [a,*], Rens Florian van der Vleuten [a], Saba Najjari Hagh [a], Sian Jones [a], Mahnaz Aghajanloo [a], Manon Arianne Renée Schellart [a], Diederik Boersma [a], Denis Voskov [a,b], Rouhi Farajzadeh [a,c]

[a] Delft University of Technology, Department of Geoscience and Engineering, Stevinweg 1, Delft 2628 CN, the Netherlands
[b] Energy, Science and Engineering, Stanford University, USA
[c] Shell Global Solutions International B.V., Grasweg 31, Amsterdam 1031 HW, the Netherlands

ARTICLE INFO

Keywords:
CO_2 storage
Rock heterogeneity
Capillary-driven backflow
Core-flooding experiment
CT scanning

ABSTRACT

Carbon dioxide (CO_2) storage in geological reservoirs is an effective approach to mitigate greenhouse gas emissions. However, salt precipitation induced by dry CO_2 injection can reduce injectivity, thereby affecting storage efficiency and operational stability. This study investigates the impact of rock permeability on halite precipitation patterns and their influence on CO_2 injectivity through core-flooding experiments. Using four distinct cores, three homogeneous and one heterogeneous under controlled conditions, we analyse the dynamic processes of brine displacement, water evaporation, salt accumulation, and permeability evolution with real-time computed tomography (CT) imaging and multiple fluid pressure sensors. Results indicate that permeability contrast redistributes brine and changes the location of salt deposition. Permeability impairment is not governed by initial permeability alone; instead, it reflects the combined influence of permeability, porosity, mineral heterogeneity, capillary retention, and local flow-path blockage. Salt precipitation is more dispersed in heterogeneous cores compared to homogeneous cores, where under our experimental conditions, it predominantly accumulates near the injection point. Furthermore, permeability impairment varies with initial rock properties, with higher-permeability cores experiencing more severe injectivity reduction due to increased pore clogging. These findings highlight the importance of incorporating reservoir heterogeneity in predictive models for CO_2 storage operations. Understanding the dynamic interplay between brine migration, salt crystallization, and permeability evolution is crucial for optimizing long-term injectivity and ensuring the viability of geological carbon storage.

1. Introduction

Carbon capture and subsurface storage (CCS) plays a crucial role in mitigating greenhouse gas emissions, particularly carbon dioxide (CO_2), which is the largest contributor to climate change [16]. In recent decades, several large-scale carbon capture and storage (CCS) projects have been developed worldwide, including the Sleipner and Snøhvit projects in Norway, the In Salah project in Algeria, and the Quest project in Canada [10,31]. These projects demonstrated the technical feasibility of CCS and provided valuable data on CO_2 storage capacity, injection rates, and monitoring techniques. In order to efficiently keep CO_2 underground for the long term, different types of geological formations serve as potential reservoirs for CCS, such as depleted oil and gas reservoirs, saline aquifers, and basalt formations [1,24].

Salt precipitation occurs in the near-wellbore area during the CO_2 injection, which introduces the risk of injection impairment [4,6,12,17,19]. [15] combined pore-scale observations, core-flood data, and field reports in a multi-scale synthesis and concluded that dry CO_2 injection dries the near-well zone and drives capillary-induced brine evaporation, which causes halite precipitation at the advancing dry-out front; [26] recently reported that the Quest CCS site in Canada had a reduction in CO_2 injectivity due to salt precipitation in the wellbore. The invading CO_2 pushes the mobile water in the reservoir away from the injection well. As water gradually evaporates into CO_2, the salinity of formation water increases until it reaches the supersaturation point of salt. Salt starts to crystallize and accumulate inside the pores, which has

* Corresponding author.
E-mail address: l.yan@tudelft.nl (L. Yan).

https://doi.org/10.1016/j.ecmx.2026.102070
Received 20 March 2026; Received in revised form 15 June 2026; Accepted 16 June 2026
Available online 17 June 2026
2590-1745/© 2026 The Author(s). Published by Elsevier Ltd. This is an open access article under the CC BY license (http://creativecommons.org/licenses/by/4.0/).

the potential of partially or completely blocking local pores and reducing the initial permeability. [9] reported a porosity reduction of 6 % and permeability impairment of 70 % in a core flooding experiment under a 25 wt% NaCl brine environment. They observed that salt crystals clogged the pore spaces and aggregated around rock grains. [33] systematically described the dynamic process of halite precipitation in the pores with homogeneous and heterogeneous grain structures. They captured that salt could reduce the maximum 15 % porosity in the microfluidic system and illustrated the impacts of CO_2 injection direction and capillary-driven backflow on salt aggregation in the porous domain.

The heterogeneity of rock permeability mainly affects two aspects: non-uniform CO_2/water distribution during CO_2 displacement and capillary-driven water backflow caused by capillary pressure gradient [30]. As schematically shown in Fig. 1, dry CO_2 injection causes three zones in the reservoir: dry-out zone, unsaturated zone and brine-saturated zone. With water evaporation, water diffuses into the dry CO_2 flow, which leads to a brine saturation gradient across the dry-out front [14]. That in turn results in capillary-driven backflow of water from water clusters in the unsaturated zone towards the dry-out zone [7]. Some studies proposed that the salt patterns depend on a critical flow rate, below which capillary forces dominate the viscous forces [8,20,34]. When the flow velocity of CO_2 exceeds the critical velocity, salt precipitates uniformly at the macroscopic scale. When the velocity is below the critical threshold, capillary pressure induces the backflow of residual brine, transporting solutes towards the injection point, where salt ultimately precipitates. However, few studies have proved this theory through direct experimental observations and there is no comprehensive model for defining the critical flow rate [6,29].

On the other hand, the reservoirs naturally contain complex permeability of sedimentary formations, giving rise to the issues in the variation of capillary pressure corresponding to the permeability, from the perspectives of both microscopic and macroscopic scenarios [21,22,27]. During the CO_2 displacement, CO_2 flow enters more of the high-permeability layer (yellow region marked with ‘high k’ in Fig. 1) due to the lower capillary pressure in the high-permeability layer. A capillary pressure gradient can occur between the two layers with different permeability, which induces water movement from the low permeability layer to the high permeability layer [25]. It is considered as the capillary-driven crossflow between heterogeneous layers. However, the influence of permeability on the salt precipitation and its distribution, and their impact on injectivity still need to be investigated. Systematic experimental and numerical investigations are required to elucidate the quantitative relationships between reservoir heterogeneity parameters and salt precipitation dynamics.

The objective of this study is to examine how rock permeability affects salt precipitation behavior, its spatial distribution, and the changing injection pressure during CO_2 injection. Four core samples are used, with permeabilities ranging from 0.1 to 2 Darcy. Three of these cores are natural outcrop samples with relatively uniform pore and permeability distributions, while the fourth is an artificially created core designed to show a heterogeneous pore structure. To observe the salt precipitation process in real time, a medical CT scanning system is set up in the laboratory. This setup allows for detailed monitoring of the location of salt deposition, providing useful insights into the interactions between brine, CO_2, and the porous medium.

2. Experimental methods and materials

1.1. Experimental setup

Fig. 2 illustrates the experimental setup designed to investigate the salt dry-out process during CO_2 injection in porous media and used for the work described in this report. The system integrates a high-pressure CO_2 injection apparatus, a medical X-ray CT scanner, and a rock sample placed inside a core holder for dynamic imaging and pressure monitoring. The scanner is the Siemens SOMATOM third-generation CT scanner with a voxel size of 23,000 μm^3, which enables real-time 3D imaging of fluid distribution and salt deposition.

On the left side of the figure, dry CO_2 with 99.7 % purity is supplied from a gas cylinder (1) and regulated through a Bronkhorst EL-FLOW mass flow controller before being injected into the rock sample. The CO_2 flows through the core holder (6), displacing brine and causing water evaporation, which leads to salt precipitation. The temperature is controlled by using a heating jacket (4) around the core holder. The core holder is placed inside a CT scanning unit (2) that can capture high-

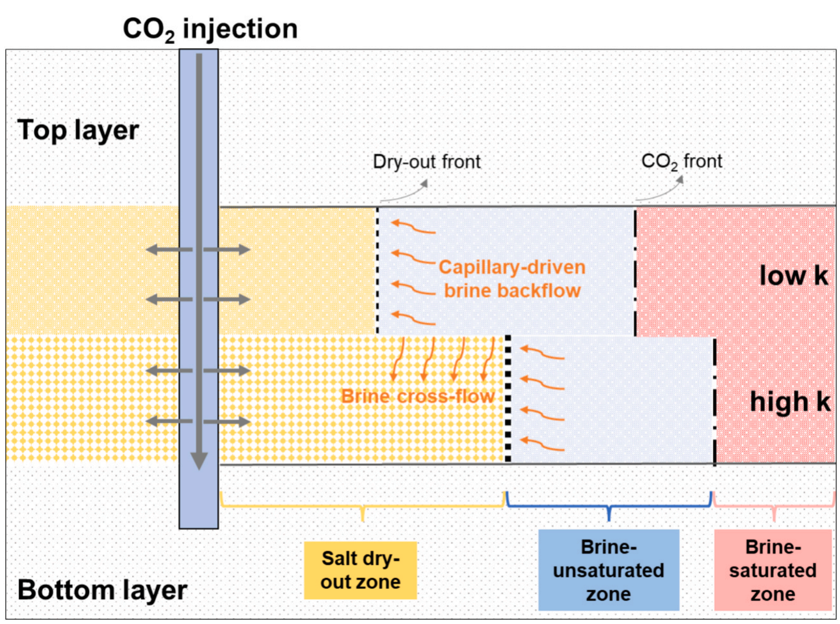

Fig. 1. Schematic of the capillary-driven backflow during CO_2 injection. Three zones, the salt dry-out zone, CO_2-brine unsaturated zone, and brine-saturated zone, appear after CO_2 injection into the two reservoir layers with low and high permeability, which are indicated by using three colours, yellow, blue, and red, respectively. The horizontal orange arrows represent the capillary backflow due to the capillary pressure gradient, and the vertical arrows represent the capillary pressure difference between layers. (For interpretation of the references to colour in this figure legend, the reader is referred to the web version of this article.)

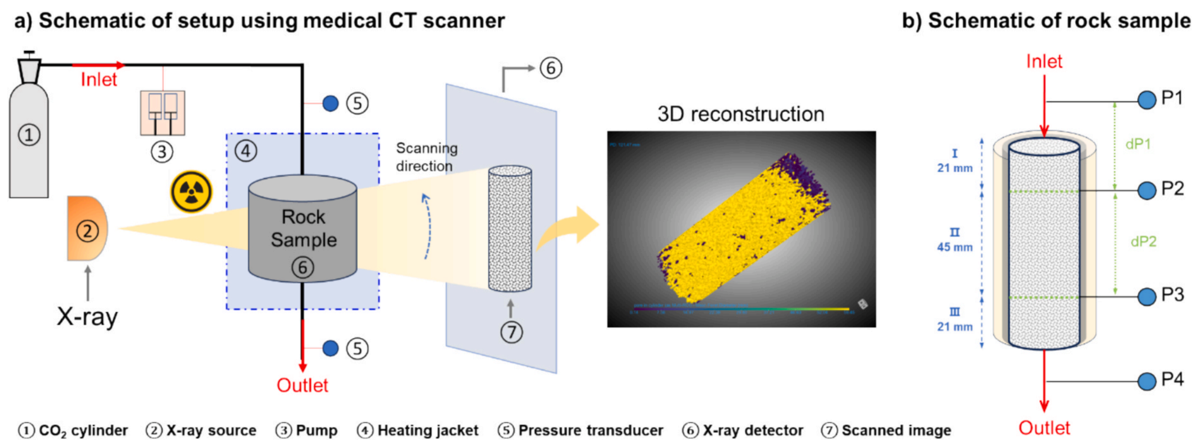

Fig. 2. Schematics of experimental setup and the rock core. a) The connection of the CO_2 injection system with the real-time CT imaging unit. An example of 3D reconstructed CT image of the rock core is provided. b) A schematic representation of the rock core and holder, along with differential pressure monitoring points (dP1 and dP2).

resolution images within 5–10 s by emitting X-ray beams through the sample. The transmitted signals are processed to reconstruct detailed cross-sectional images, enabling real-time monitoring of salt precipitation dynamics. The right section of Fig. 2a) presents a 3D reconstructed CT scan of the core, where darker and yellow regions indicate precipitated salt and remaining pore spaces in the figure, respectively. In Fig. 2b), a schematic of the rock sample details its segmentation into three regions for the pressure monitoring: the inlet section (21 mm), middle (45 mm), and outlet section (21 mm). Four pressure sensors (P1–P4) and two differential pressure sensors (dP1 and dP2) are positioned along the core to track real-time pressure changes. These differential pressures can be used to calculate the permeability for the three sections reflecting the dynamic permeability changes during salt precipitation. The labelled inlet and outlet directions emphasize the CO_2 flow path. The grey layer is the glue of the core to prevent the water from entering the core, and the transparent-yellow layer is the core holder made by PEEK plastic (polyetheretherketone). The core is placed in a vertical position to reduce the influence of gravity on the salt pattern. We use one injection cap with one middle injection point in this work. Compared with a uniform distributor, this geometry makes the location of the drying front and inlet-proximal salt accumulation easier to identify in CT images. This setup enables dynamic visualization of salt precipitation patterns, providing crucial insights into how salt accumulation affects rock permeability and CO_2 injectivity.

1.2. Experimental conditions and core properties

In order to investigate the effect of heterogeneity on the salt precipitation, four cores with various permeabilities were used. Fig. 3 presents the core samples used in the experiments, including both homogeneous and heterogeneous configurations. The homogeneous core samples consist of Bentheimer, Berea, and Fontainebleau sandstones, each shaped into a cylindrical geometry with a 40 mm diameter and 87 mm length.

The homogeneous sandstone cores exhibit relatively uniform internal structure with a lower than two-times difference of heterogeneity in horizontal and vertical permeability along the cores. These cores enable the assessment of salt precipitation and CO_2 flow dynamics under well-known uniform permeability conditions. The heterogeneous core comprises a dual-layer structure with an inner Fontainebleau outcrop core embedded within an outer Fontainebleau sand layer. The heterogeneous sample should be regarded as a radial permeability contrast rather than a direct mimic to a laterally layered reservoir. When the sample is prepared, CT scanning can be used to check the contact between the inner and outer layers and make sure that there are no obvious gaps along the cylindrical interface. The sand layer is grinded and packed from the same rock as the inner outcrop core. The inner layer features a permeability of 160 mD, whereas the outer layer exhibits a high permeability due to the manual packing. We did not separately measure the permeability for the outer sand layer but measured the average permeability (5243 mD) after packing the heterogeneous core. The inner core radius measures 12.5 mm, and the total composite radius extends to 25 mm, which allows for emphasizing the effects of permeability variation on brine displacement and salt precipitation patterns.

To prevent flow bypassing and ensure controlled CO_2 injection, epoxy resin fully encapsulates each core sample, as shown in the grey region of the homogeneous core. The injection port is positioned at the center of the core, directing CO_2 into the core.

Table 1 summarizes the permeability, porosity, pore size, and injection conditions for different core samples used in the experiments.

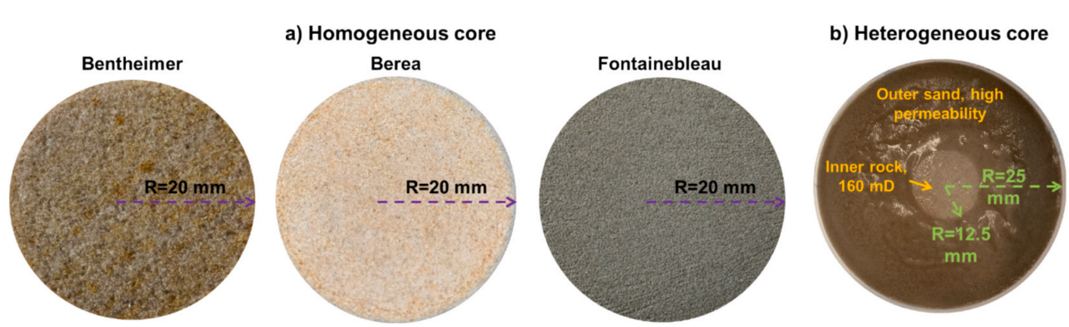

Fig. 3. Comparison of homogeneous and heterogeneous core samples. (a) Homogeneous cores with a uniform structure and a radius of 20 mm. (b) Heterogeneous core consisting of an inner Fontainebleau outcrop core (160 mD permeability, radius 12.5 mm) and an outer Fontainebleau sand layer (radius 25 mm). The heterogeneous core is saturated with water for distinguishing the different rock regions.

Table 1
Core sample properties and experimental conditions.

Core type	Brine permeability (mD)				Porosity	Core length (mm)	Brine	Injection rate (mL/min)
	Section I	Section II	Section III	Total				
Bentheimer	2164	1707	1393	1950	0.22	87	25 wt% NaCl	15
Berea	161	165	175	166	0.18			
Fontainebleau	164	187	155	152	0.10			
Heterogeneous	–	–	–	5243	0.21 (averaged)	67		6
Working conditions: atmosphere pressure and 50 °C.								

The table presents sectional permeability values for each core, highlighting variations along the sample length. The Bentheimer core exhibits high, anisotropic brine permeability (Section I: 2164 mD, II: 1707 mD, III: 1393 mD; total: 1950 mD), while the Berea core shows uniformity across sections (161–175 mD, total: 166 mD). Fontainebleau displays moderate permeability (155–187 mD, total: 152 mD). The porosity of Bentheimer and Berea sandstones is similar (0.22 and 0.18, respectively), while Fontainebleau sandstone has a significantly lower porosity (0.10), indicating a more compact pore network. The experiments employ a 25 wt% NaCl brine for all cores as a high-salinity brines relevant to CO_2 storage in saline aquifers [11,32]. Injection rates are tailored to core permeability heterogeneity: 15 mL/min for the homogeneous core ensures capillary numbers (the ratio of viscous force and the surface tension force, Ca $\approx 10^{-11}$) within capillary-dominated flow regimes, while the heterogeneous composite core operates at 6 mL/min to maintain the stable position of sand in the outer layer. Stepwise rate increments (7 steps within one hour injection) under 50 °C and atmospheric pressure prevent flow shock and stabilize capillary equilibria. At atmospheric pressure, CO_2 density, water-carrying capacity per unit pore volume, viscosity, diffusivity, and phase behavior differ strongly from reservoir conditions. The absolute drying rate and the number of injected pore volumes required for complete desiccation are therefore not directly transferable to deep storage reservoirs, where CO_2 may be dense or supercritical. Every experiment has been conducted twice for checking the repeatability.

The mineralogical composition and pore structure of rock samples play a crucial role in controlling capillary pressure and fluid flow behaviour. Fig. 4a) presents a comparative analysis of mineral composition, pore structure, and capillary pressure-water saturation relationships for Fontainebleau, Bentheimer, and Berea sandstones, providing insights into their permeability characteristics and fluid flow behaviour. The bar chart on the left illustrates the mineralogical composition, where Fontainebleau sandstone exhibits the highest SiO_2 content (~99 %), indicating a highly mature quartz-dominated structure with minimal impurities, resulting in low chemical reactivity and excellent permeability stability. Berea sandstone, in contrast, contains only 85 % SiO_2 with significant amounts of Al_2O_3 (~6 %) and K_2O (~4 %), suggesting a higher presence of feldspar and clay minerals. Bentheimer sandstone, with 97 % SiO_2, lies between the two in terms of mineral purity and flow properties. Fig. 4b) depicts the capillary pressure (P_c)-water saturation (S_w) relationships. We, therefore, focus the analysis of experiment on the combined effect of pore-scale heterogeneity in the cores with the average permeability. [18] demonstrated that the heterogeneity in rock porosity determines the distribution of salt deposits and observed the capillary-driven transport of brine at the pore-scale. Fontainebleau sandstone, characterized by large, well-connected pores, exhibits the lowest capillary pressure at any given water saturation, indicating efficient drainage, low irreducible water saturation, and high CO_2 displacement efficiency. In contrast, Berea sandstone, with its heterogeneous pore structure and finer grains, shows significantly higher capillary pressure, leading to stronger capillary trapping of water and greater brine retention. Bentheimer sandstone, exhibiting moderate pore size and connectivity, falls between the two, showing intermediate capillary pressure and water retention behaviour. These trends align with classical capillary scaling models, such as Brooks and Corey (1964) and van Genuchten (1980), which describe how pore size distribution and wettability influence fluid displacement efficiency. The observed higher capillary pressure in Berea sandstone confirms a tighter pore network with stronger capillary forces, making it more susceptible to salt precipitation and CO_2 injectivity impairment, whereas Fontainebleau's low P_c enables more efficient CO_2 migration.

1.3. Experimental procedure

The experiments are conducted in several stages to maintain consistent conditions. We begin with general preparation, including

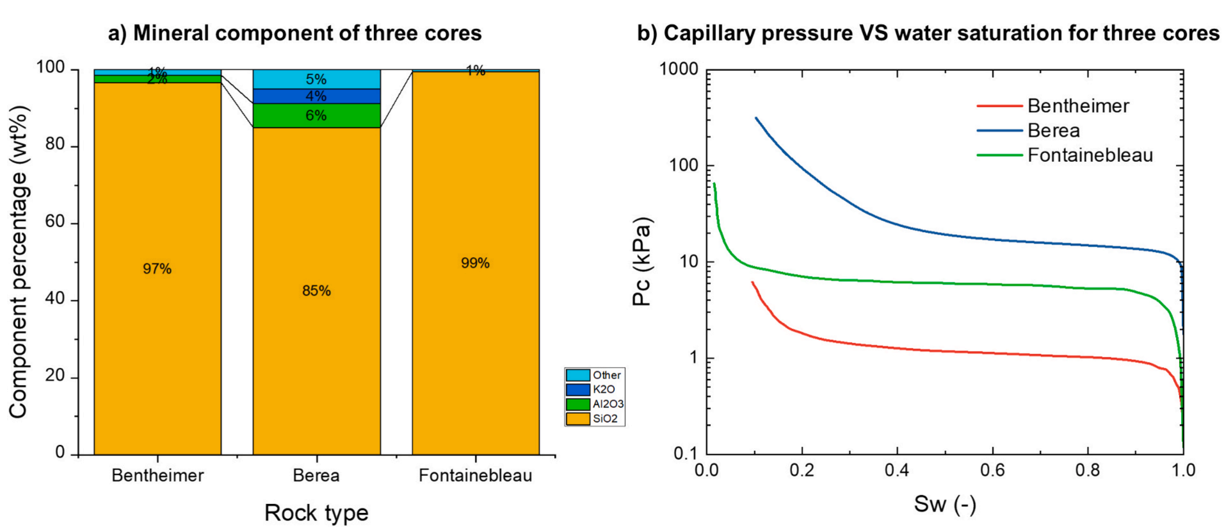

Fig. 4. Comparison of mineral composition and capillary pressure-water saturation relationships for Bentheimer, Berea, and Fontainebleau sandstones [3,5,13].

mixing brines at the required salinity and degassing them to eliminate trapped air. Then, we install the core sample into the core holder and drill the differential pressure (dP) measurement ports on the holder. After setting up the entire system, we perform a helium leak test to make sure the system is leak-free. The basic procedures for the whole experiment are listed below:

- CO_2 saturation stage: the core is first saturated with CO_2 at a constant flow rate of 15 mL/min for approximately five pore volumes (PV). We then carry out a CO_2 permeability test at different flow rates. Since the experiment is performed at atmospheric pressure, gas compressibility effects can be neglected.
- Brine saturation stage: For brine saturation, we initially inject a low-salinity brine (1 wt% NaCl) with a flow rate of 5 mL/min for 3 PV and connect the system to a vacuum pump to make sure the core can achieve almost full brine saturation. After the core is fully saturated, we close the outlet valve to allow pressure to build above atmospheric levels and set the backpressure to 10 bar to dissolve remaining gas in the brine. The brine permeability test is performed using the low-salinity brine. We then inject high-salinity brine to prepare the core for at least 20 PV to fully saturate core with high-salinity brine. After brine saturation, the outlet was connected to the downstream tubing and maintained at atmospheric pressure during CO_2 injection; no back-pressure regulator was used. Prior to CO_2, a brine retraction about 10 cm away from the inlet port is conducted to minimise the risk of salt precipitation near the injection zone.
- CO_2 flooding stage and dynamic CT scanning: Once brine saturation is completed, the system is depressurized back to the room pressure and 50 ℃ controlled by the heating bath. CO_2 is injected, and the flow rate is gradually increased in steps to avoid flow shocks until reaching the required value. CO_2 injection is kept in the entire experiment. During the flooding experiment, the system is monitored for pressure, and real-time imaging is conducted using a CT scanner. These imaging results are processed to analyse porosity changes, saturation distributions, and permeability reductions caused by salt precipitation.

The details of data and image processing are described in the Supplementary material.

3. Results and discussion

1.1. *Typical behaviour of dynamic halite precipitation in homogeneous rock*

This section provides a detailed presentation of one representative case from the six homogeneous core flooding experiments, specifically the Berea outcrop sandstone. The rest of the results of experiments in the Bentheimer sandstone and Fontainebleau sandstone are shown in the Supplementary material. CT scanning enables precise monitoring of the spatial and temporal evolution of salt precipitation, including its distribution and morphology.

Fig. 5 illustrates the final salt deposition at the top surface of core as well as the dynamic progression of salt precipitation during CO_2 injection. In Fig. 5a), the white granular structures represent precipitated salt, which is predominantly located near the inlet region and exhibits a circular radial pattern. This distribution indicates that salt precipitation intensifies closer to the injection point, which is further confirmed by the false-colour images, where higher salt concentrations correspond to increased density, resulting in stronger red intensities (higher Hounsfield units). The CT images at different injection times in Fig. 5b provide additional validation of this trend. These images are based on original CT scans with color mapping applied to differentiate materials of varying densities, enhancing the visualization of salt deposition patterns without altering the raw data structure. The yellow regions in the central part of the core are due to the selection of a single CT scan slice, where large pore spaces result in lower grayscale values (1270) compared to denser salt particles (1685). Initially, the core appears predominantly blue, representing low-density air-filled pore space in its dry state. Upon saturation with a 25 wt% NaCl brine solution, the pores become filled with high-salinity brine, shifting the colour representation toward red. After 10 pore volumes (PV) of CO_2 injection, brine displacement is evident, yet capillary end effects cause residual water to accumulate at the bottom of the core. As the injection progresses to 508 PV, a noticeable reduction in brine volume occurs, accompanied by salt precipitation at the centre top of the core (manifested as a protrusion at the rock boundary in red). At 1471 PV, a significant reduction in residual water at the bottom of the core is observed. With continued salt precipitation at the top, by 4300 PV, the core has undergone complete drying, and salt accumulation remains concentrated near the injection inlet. The findings suggest that capillary-driven backflow plays a crucial role in transporting brine upward, overcoming gravitational forces, and contributing to the salt deposition pattern. The salt likely accumulates more on the surface of the middle core at middle region due to the dry

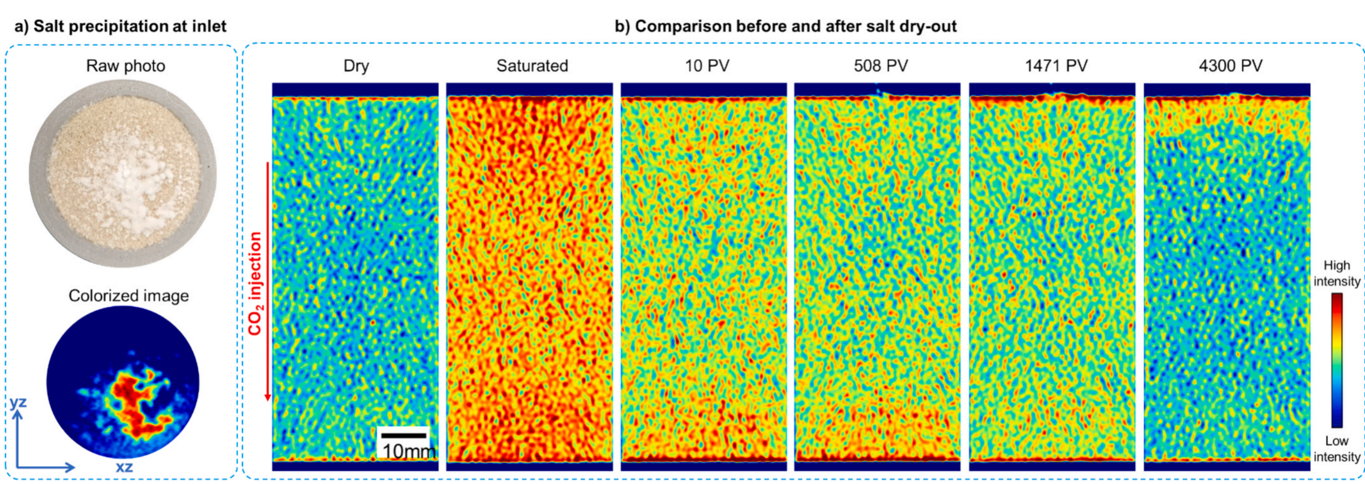

Fig. 5. Images of dynamic salt precipitation process in the Berea core. (a) shows a top-view image of the core after complete salt precipitation, where the white regions in the upper image correspond to solid salt deposits. (b) illustrates the evolution of salt precipitation during CO_2 injection, depicting the spatiotemporal distribution of salt formation.

gas coming first from the middle injection point. Segmented salt-phase images for different cores can be found in Section 3.3, where a more detailed quantitative analysis is provided.

Fig. 6 illustrates the dynamic changes of CO_2 saturation and porosity along the Berea core during CO_2 injection experiment. Following CO_2 injection, water saturation is non-uniform from the top to bottom of the core. In the bottom section of the core (70–83 mm), water saturation remains close to 80 % due to the capillary-end effect (highlighted in the red rectangular box) [2]. In contrast, in the upper section of the core (0–35 mm), the average CO_2 saturation reaches 0.48, while in the middle section (35–70 mm), it stabilizes at 0.43. During the initial injection phase (10–100 pore volumes (PV)), a noticeable increase in CO_2 saturation occurs in the top and bottom sections of the core (0–70 mm), with an average increment of 0.1 % and a growth rate of 4.3×10^{-4} per PV. In the subsequent injection period (100–508 PV), the rate of CO_2 saturation increase slows down due to the water evaporation, with average saturations of approximately 0.6 in the upper section and 0.5 in the middle section. The average rate of CO_2 saturation increases further, then declines to 6.8×10^{-5} per PV, which is also the water evaporation rate into the CO_2 stream. Between 508 and 4300 PV, salt precipitation becomes obvious at the top of the core (0–15 mm), leading to a notable decline in CO_2 saturation because of the pore blockage. As water gradually evaporates, the salt front advances deeper into the core. It should be noted that the plotted saturation profiles are not uniformly spaced in injected pore volumes. Once salt precipitation became visible near the inlet, the CT scanning interval is increased because the following analysis focuses on permeability evolution before and after salt formation and on the final dry-out state. Therefore, the transition from 1815 PV to 4300 PV represents a large accumulated injection interval rather than an instantaneous jump between two adjacent scans. Meanwhile, in the middle section (35–70 mm), CO_2 saturation continues to increase slowly but steadily, with an average rate of 1.2×10^{-4} per PV. This value is 1.9 times higher than it was in the previous injection period, which is consistent with the observation in our other work in the micromodel [33]. A significant rise in CO_2 saturation is also observed at the lower section of the core (70–83 mm), where the water saturation depletes. By 4300 PV, the zone of reduced CO_2 saturation at the core top extends to a depth of 15 mm, indicating that the salt front has propagated to this depth. In the remaining sections of the core, CO_2 saturation approaches 1.0, signifying complete drying of the core.

Additionally, based on image analysis and measured CO_2 saturation data, a dynamic porosity evolution curve is generated, as depicted in Fig. 6b. Overall, the porosity distribution remains relatively uniform without significant large-scale heterogeneity. The initial average porosity of the rock is 0.18, with slightly higher values at the top (0–15 mm) and bottom (70–83 mm), while the rest of the core maintains a porosity of 0.175. At the final condition of salt dry-out, the variation in porosity aligns closely with changes in CO_2 saturation. Upon complete drying of the core, a significant porosity reduction is observed in the top section, where it declines from 0.18 to 0.05 due to salt deposition. The extent of porosity reduction gradually decreases between 5–15 mm, eventually approaching the initial porosity value. Salt precipitation is primarily concentrated near the injection point, and no significant porosity reduction is observed in the rest of the core.

Fig. 7 presents the differential pressure evolution across two sections of the core during CO_2 injection, which reflects the impact of salt precipitation on flow dynamics. The dark grey curve represents core Section 1 (0–21 mm), while the green curve corresponds to core Section 2 (21–65 mm). Section 2 shows an initial pressure response associated with gas breakthrough and then stabilizes rapidly, indicating that the main connected gas pathway in the downstream section was established early. In contrast, Section 1 shows a gradual step-wise pressure increase before approximately 500 PV. We interpret this early response as an inlet-proximal resistance evolution caused by brine redistribution, evaporation-induced salinity increase, incipient salt crystallization and intermittent local pore/throat obstruction near the injection region. After approximately 500–600 PV, a sharper pressure increase becomes visible, concurrent with the onset of detectable salt precipitation near

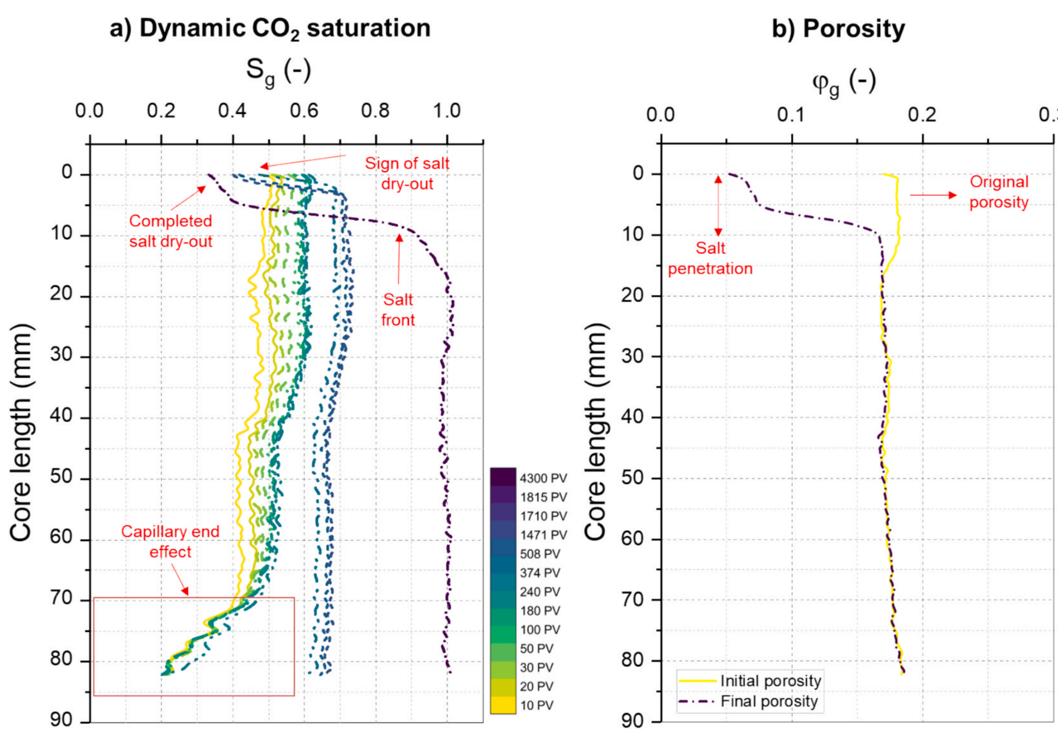

Fig. 6. Evolution of salt precipitation and porosity reduction of Berea core during CO_2 injection. a) shows dynamic saturation of CO_2 along the core. The colour of curves from yellow to blue represents the increasing injection time. b) shows the core porosity at initial and final conditions. The porosity reported in this study is not the intrinsic rock porosity. It is a CT-derived proxy of porosity. (For interpretation of the references to colour in this figure legend, the reader is referred to the web version of this article.)

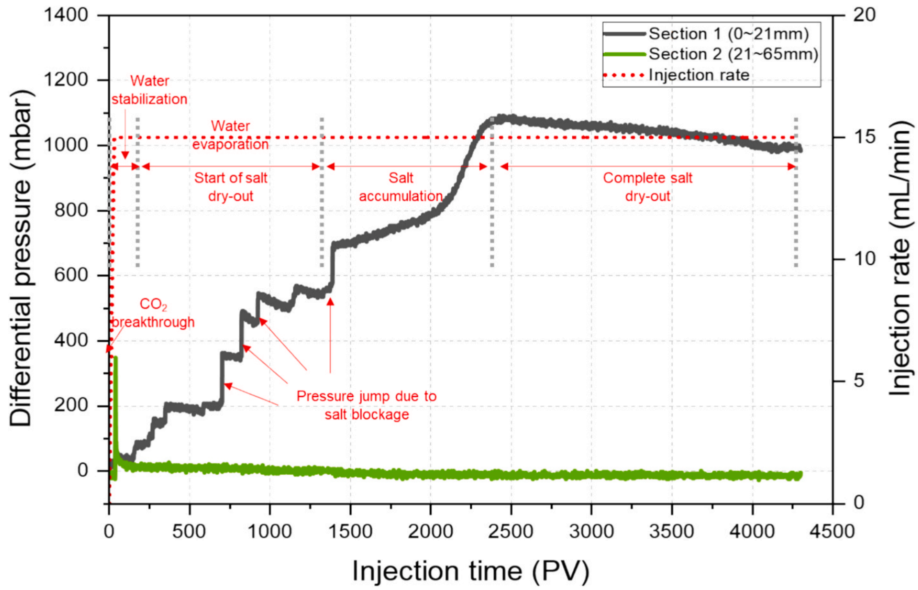

Fig. 7. Profile of differential pressures for the Berea core. The dark charcoal and green curves present the pressure change of Section 1 (0–21 mm) and Section 2 (21–65 mm) of the core, respectively. The flow rate is shown in the red-dotted curve. (For interpretation of the references to colour in this figure legend, the reader is referred to the web version of this article.)

the inlet. This indicates that early local restrictions gradually evolved into more significant salt-induced blockage of primary flow pathways. Between 1400 PV and 2000 PV, the pressure begins to rise gradually, and salt precipitation progressively reduces permeability near the inlet. This trend intensifies between 2000 PV and 2300 PV, where the pressure increase accelerates. We attribute this to rapid pore blockage, which further restricts flow and indicates that salt crystallization is driving further porosity reduction and permeability impairment. After 2300 PV, the differential pressure starts to decrease, which indicates that residual water is evaporating and most of the salt has already precipitated. In the final injection stages, the pressure stabilizes and salt dry-out is nearly complete. In addition, the stable pressure profile in section 2 confirms that salt precipitation is largely concentrated near the inlet (section 1), where brine evaporation and capillary effects play a dominant role in precipitation patterns.

We present the 3D reconstruction of salt distribution along the three homogeneous cores, as shown in Fig. 8. It is worth noting that 3D reconstructions capture only the internal rock volume of the cores and do not include the salt that accumulated on the external top surface. The surface salt accumulation is instead visible in the photographs and colorized 2D projections (as shown in Fig. 5 and the Supplementary Material). The 3D reconstruction of salt in the heterogeneous core is not shown in this paper, due to low contrast between the low-permeability rock and salt which causes difficulty in distinguishing in the low-permeability region. Overall, the high-permeability Bentheimer core exhibits a more continuous and internally distributed salt accumulation, with obvious salt presence extending from the top towards the bottom of the core. As permeability decreases, salt precipitation increasingly localizes at the external surface rather than within the core interior. Consequently, both the Berea and Fontainebleau cores display a “ring-like” salt accumulation pattern at the top section of the cores. This annular morphology is particularly pronounced in the Fontainebleau core, where precipitation is more strongly concentrated at the surface and the apparent thickness of the salt “ring” is smaller. This behaviour is possibly attributed to the lower porosity of the Fontainebleau sandstone (~0.10) compared with the Berea core (~0.20). In addition, a distinct internal annular salt band is observed in the midsection of the Berea core. This band coincides with a relatively dense lamina that is intrinsically less permeable than the surrounding rock. However, Bentheimer has a more open and connected pore network with more permeable and variable across sections. Therefore, salt precipitation is distributed more continuously along the upper part of the core instead of forming a narrow internal band. During CO_2-brine displacement, capillary forces promote enhanced brine trapping within this layer, which ultimately leads to preferential salt precipitation and formation of the ring-shaped band. Salt accumulation is also observed at the downstream end (bottom) of the core, where the capillary-end effect causes brine retention and the subsequently localized salt clustering.

1.2. *Typical behaviour of halite precipitation in heterogeneous rock*

The core contains the inner cylindrical rock with a lower permeability of Fontainebleau (160 mD) and the outer layer of well-grinded sand from Fontainebleau rock (~2000 mD). The experimental conditions are the same as those in the homogeneous cores: 50 ℃ and atmospheric pressure.

Fig. 9 illustrates the dynamic evolution of salt precipitation in a heterogeneous core. Fig. 9a) presents top-down views of the core after salt dry-out, showing a circular salt deposition pattern with a high-density ring near the center of the core. Unlike the homogeneous core in Fig. 5a), the heterogeneous core exhibits a higher amount of salt accumulated, which implies that salt dry-out and water redistribution processes are influenced more by the permeability contrast between two core layers. Fig. 9b) provides CT images at various time points that capture the progression of salt accumulation during CO_2 injection. The colorized CT images represent relative X-ray attenuation rather than permeability directly. In the initial brine-saturated state, the low-permeability inner sandstone shows a higher apparent attenuation because of its denser rock framework and lower porosity, whereas the packed high-permeability sand layer has a lower bulk attenuation. High-permeability low-permeability At the early stage of injection (~50 PV), the high-permeability layer transitions to darker and lighter shades of orange, while the low-permeability core retains its red colour. This suggests that CO_2 preferentially permeates through the high-permeability layer, which has a lower entry capillary pressure compared to the inner rock. Brine retention is notably higher at the bottom of the core, influenced by the capillary-end effect. In contrast to a homogeneous core, the heterogeneous permeability structure in this scenario leads to a preferential distribution of brine towards the inner core. During intermediate stages of injection (720 and 1200 PV), salt

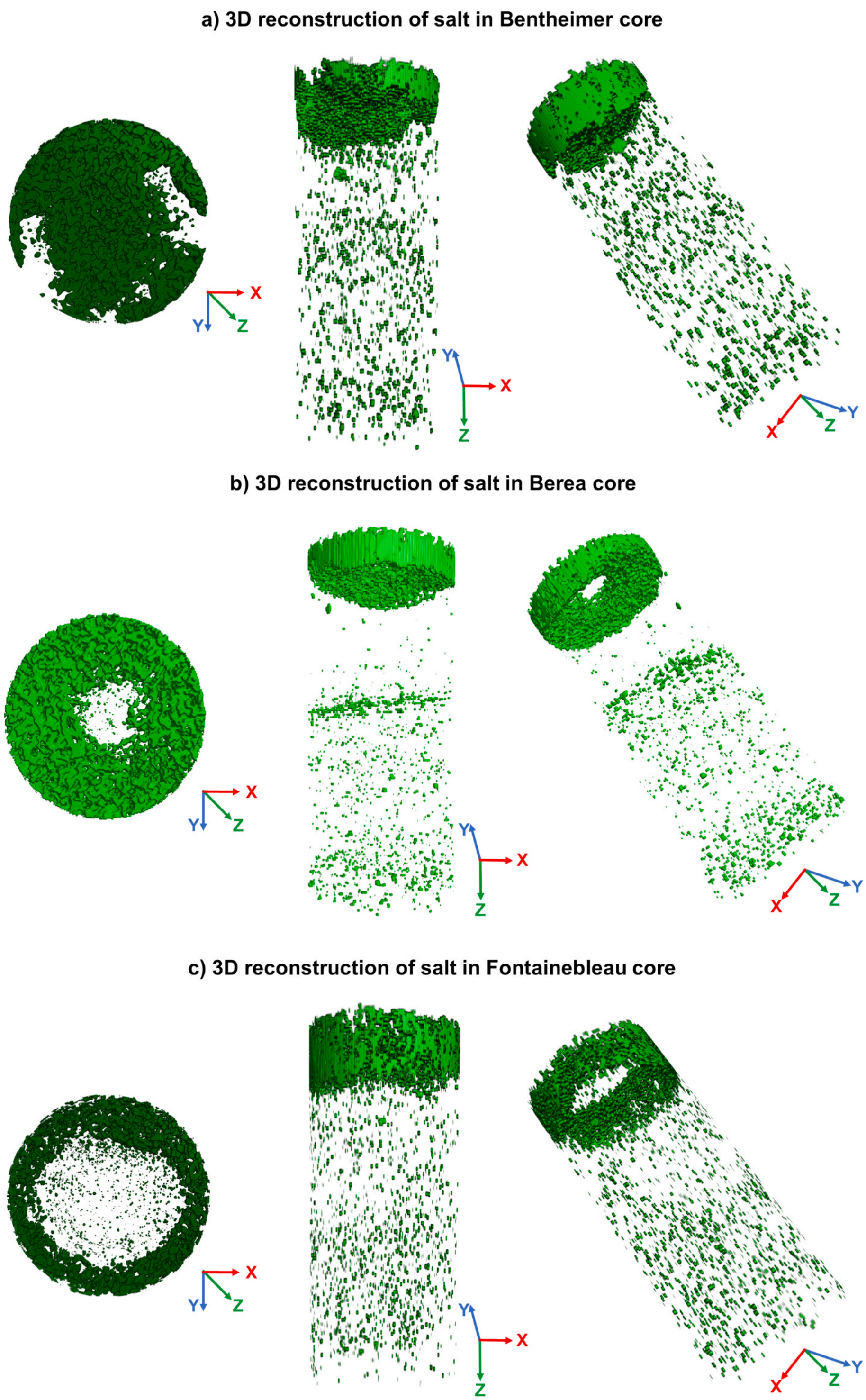

Fig. 8. 3D reconstruction of salt in three homogeneous cores.

precipitation becomes evident at the upper boundary. Instead of a uniform deposition layer seen in homogeneous cores, salt preferentially accumulates at the interface between the low-permeability and high-permeability layers, indicating that permeability contrast influences the location of precipitation. As the injection progresses, salt deposits extend upwards, with an increase in precipitation intensity. By 3000 PV of CO_2 injection, pronounced salt structures protrude at the top boundary of the low-permeability core, with the salt boundary extending towards the top of the high-permeability sand layer. However, at this stage, there is no visible advancing salt front penetrating, especially in the high-permeability layer.

Fig. 10a) delineates the spatiotemporal evolution of CO_2 saturation within the heterogeneous core assembly. Initially, the core remains fully saturated with brine. By 1 PV, CO_2 preferentially migrates through the high-permeability outer sand layer and flushes most brine at the section of 0–10 mm from the top. The rest of the core shows low gas saturation. The axial gas distribution exhibits pronounced undulations. For example, at 20–40 mm and 50–60 mm along the core, the gas saturation (Sg) reaches about 0.1, whereas other segments are near zero. With continued CO_2 injection, these contrasts sharpen. By 1200 PV (pore

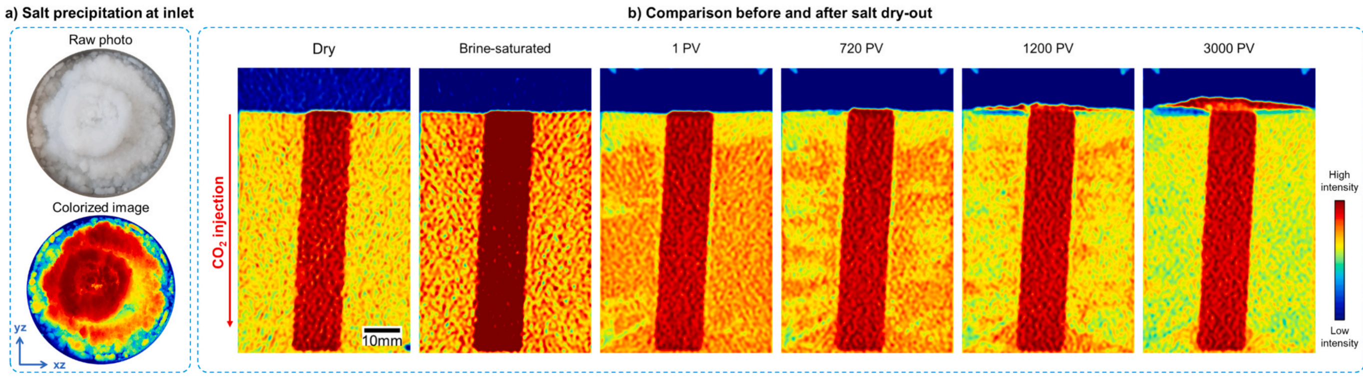

Fig. 9. Images of dynamic salt precipitation process in the heterogeneous core. (a) shows the salt patterns after the completed salt dry-out. (b) presents the dynamic processes of salt precipitation until 3000 PV injection.

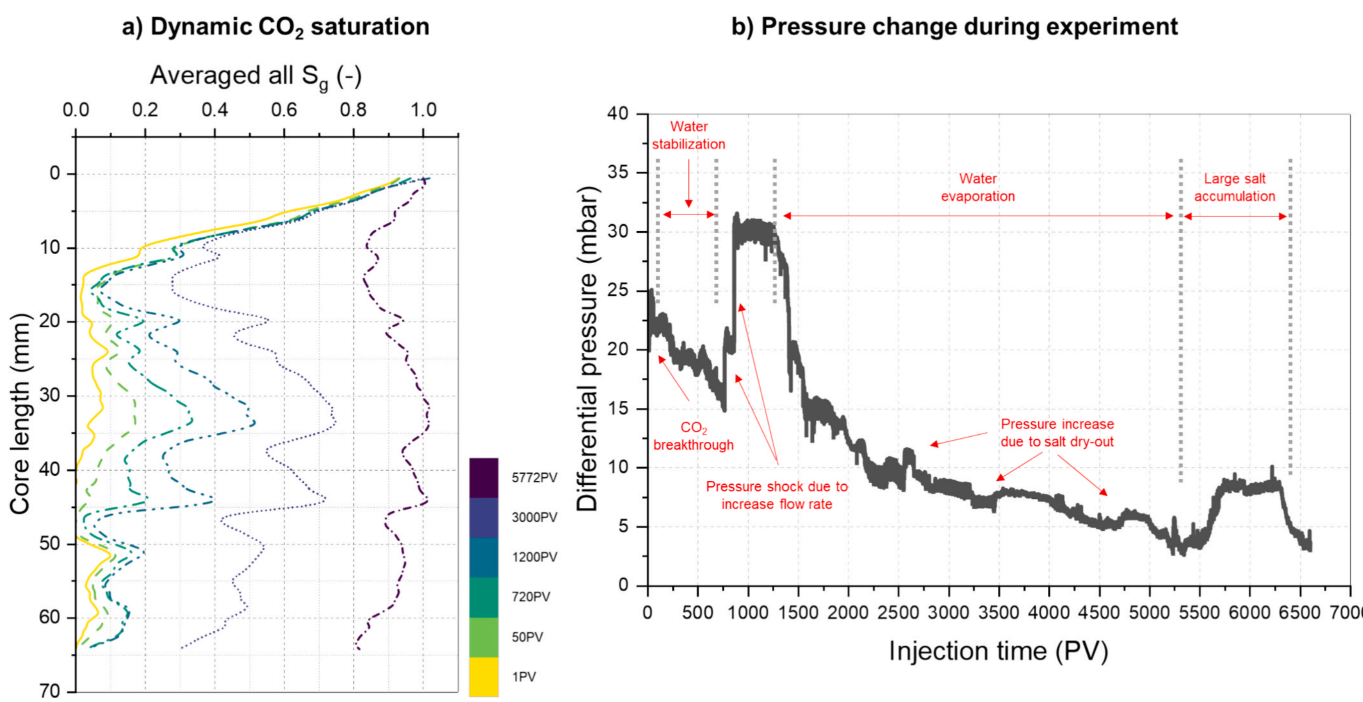

Fig. 10. CO_2 Saturation and Differential Pressure in a Heterogeneous Core. (a) gives the dynamic CO_2 saturation along the core during the experiment; (b) shows the differential pressure variation. The differential pressure is the total pressure difference between the inlet and outlet.

volumes injected), the 20–45 mm interval shows an average Sg ≈ 0.3, with a local maximum of ≈ 0.5 at 35 mm; elsewhere Sg increases only slightly. This indicates that the gas–water contact becomes progressively more stable yet strongly heterogeneous, governed by the pronounced heterogeneity of the grain framework near the outer core region. At 3000 PV, the spatial pattern persists but with higher overall Sg. By 5772 PV, parts of the 30–40 mm interval reach Sg ≈ 1, evidencing early dry-out there, while other zones, especially 10–25 mm and 45–68 mm, retain substantial water. Consistent with the CT images, this residual water is concentrated in the inner lower-permeability domains.

Fig. 10b) illustrates the differential pressure variation between the inlet and outlet, showing the effect of salt precipitation on flow resistance. In the early injection stage (0–200 PV), pressure remains relatively stable, with minor fluctuations corresponding to CO_2 breakthrough. Unlike in the homogeneous core, where pressure increases gradually as salt deposition progresses uniformly, the heterogeneous system experiences abrupt fluctuations. After 5500 PV, differential pressure begins to increase, indicating that most of the salt has precipitated and residual brine has evaporated, enhancing gas mobility. Unlike in the homogeneous core, where pressure stabilizes smoothly, the heterogeneous core exhibits prolonged pressure fluctuations, suggesting that localized salt deposits continue to restrict CO_2 flow in specific regions. One point worth noting is that a higher-permeability core takes a longer time to reach the completed dry-out conditions. Bentheimer and heterogeneous sandstones take more than two times longer to have the total dry-out than Berea and Fontainebleau sandstones.

1.3. Impact of permeability on halite precipitation

To evaluate the influence of heterogeneity on salt precipitation, we have plotted the porosity change for four cores and the salt pattern in each core, as shown in Fig. 11. The initial (yellow) and final (blue) porosity distribution along four cores in Fig. 11 a) illustrates the impact of salt precipitation on pore-filling. In the more homogeneous cores, porosity reduction is relatively monotonous, with the most significant decline near the top due to evaporation-induced salt deposition at or near the first point of contact of the injected CO_2 and the brine-filled

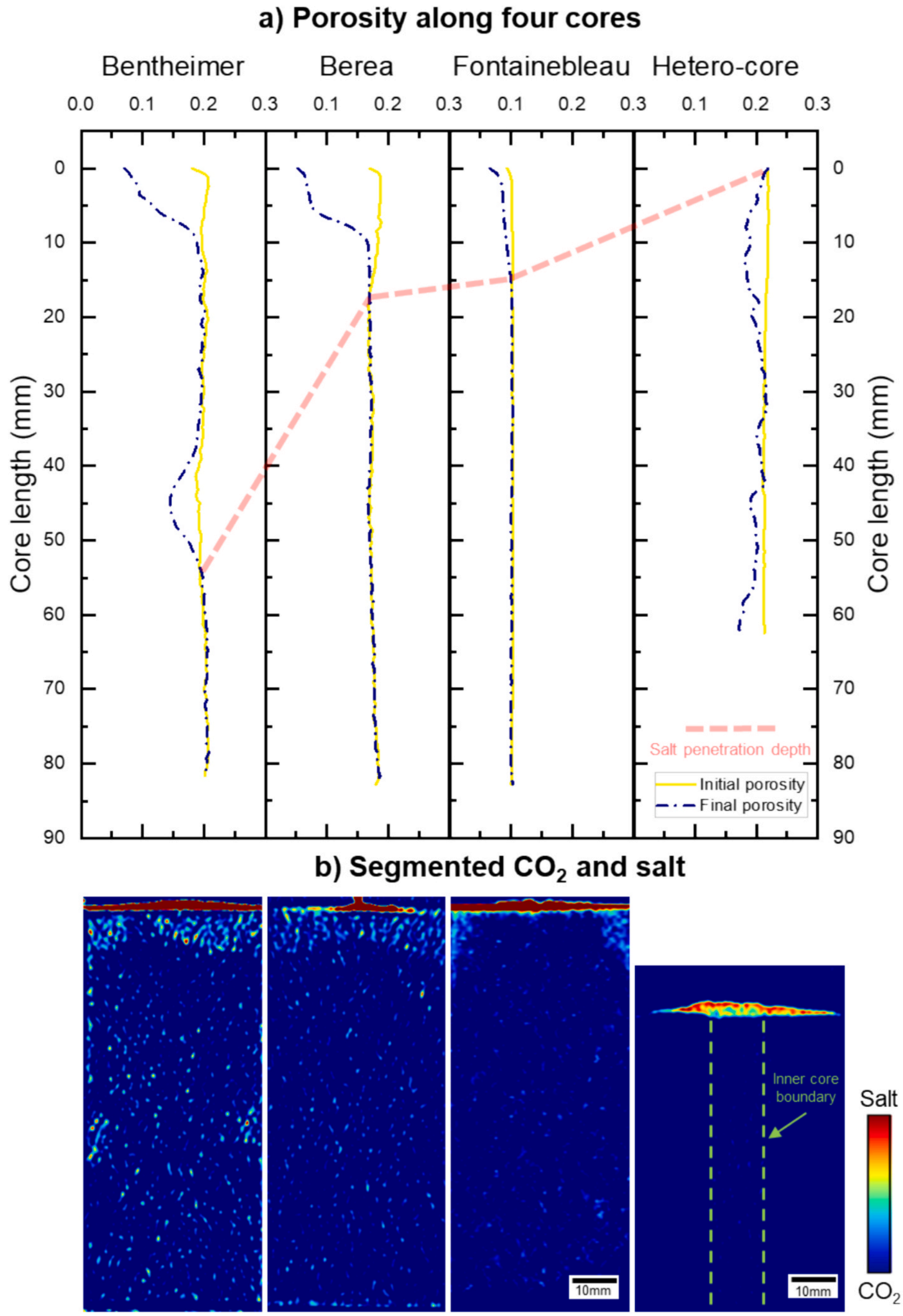

Fig. 11. Comparison of salt precipitation in four cores. (a) shows the porosity distribution along four cores. The yellow curves are the initial porosity, and the blue curves are the final porosity distribution. The porosity reported in this study is not the intrinsic rock porosity. It is a CT-derived proxy of porosity. (b) gives the segmented salt in the CT images. The red colour represents the salt, while the blue colour represents the CO_2 phase. (For interpretation of the references to colour in this figure legend, the reader is referred to the web version of this article.)

core. In contrast, highly permeable and more heterogeneous cores exhibit irregular porosity reduction, particularly near permeability interfaces where capillary-driven backflow of brine promotes localized salt accumulation. The dashed red line represents salt penetration depth, which extends deeper in high-permeability cores, as CO_2 displaces brine more efficiently, allowing salt to precipitate further into the core. One note is that the calculation of porosity in this heterogeneous core is not as accurate as in other cores due to the residual water in part of the core, which induces illusions with more porosity reduction by salt (actually, it is water) in some sections of the core. With the help of the segmented image of salt in Fig. 15b, we can determine that no visible salt penetrated the deep region of the heterogeneous core. Therefore, the dashed-red line is placed on the top of the core. Lower-permeability core (Fontainebleau) shows shallower position of salt distribution inside cores (15 mm), while higher-permeability core (Bentheimer) has the salt distribution into the 55 mm depth of the core. Notably, the hetero-core gives almost no salt penetration into the core and most salt precipitates at the surface of the core, which reflects that permeability contrast plays a key role in determining salt distribution.

Fig. 11b) presents segmented CT images, where red represents salt deposits, and blue indicates CO_2-filled pore space. Homogeneous cores exhibit continuous salt layers at the top, significantly reducing permeability and restricting CO_2 flow. In contrast, heterogeneous cores develop dispersed salt clusters, primarily forming at permeability boundaries and within low-permeability zones, suggesting that capillary effects and brine redistribution strongly influence salt precipitation patterns. This phenomenon is not observed in homogeneous cores, which also implies that enhanced brine backflow and preferential flow paths within the high-permeability sand layer contribute to localized supersaturation and accelerate salt crystallization. The final salt distribution affects CO_2 mobility, as homogeneous cores experience widespread permeability loss, creating higher flow resistance, whereas heterogeneous cores exhibit localized clogging, which may result in preferential flow pathways. These findings emphasize the importance of permeability heterogeneity in controlling salt deposition depth, distribution, and its impact on CO_2 injectivity and long-term storage efficiency.

Fig. 12 presents the relationship between normalized pressure and normalized injection time for four different cores. The normalized pressure and injection time are given by the division between the real-time values and the maximum value during injection. These plots provide insight into how permeability and heterogeneity influence pressure buildup during CO_2 injection. The distinct curves correspond to different core types. The initial pressure decrease in the heterogeneous core reflects preferential CO_2 flow through the high-permeability outer layer and brine redistribution away from connected gas pathways. This behaviour contrasts with the homogeneous cores, where the gas pathway is less strongly partitioned and pressure increases more directly once evaporation-induced salt precipitation starts to restrict inlet-proximal pores. At later times, the heterogeneous core also shows pressure buildup because salt accumulates at the permeability interface and near the injection surface. Bentheimer core occurs the increase first at about 0.1 normalized injection time. Berea and Fontainebleau cores present similar moments of starting increase in pressure. In the trend of increase, Berea shows more fluctuation in the normalized pressure compared to the other two cores, which is attributed to localized salt precipitation controlled by internal laminae and mineralogical heterogeneity. These features can retain brine locally and promote preferential halite crystallization. The subsequent partial blockage and reopening of connected pathways produce the observed pressure fluctuations. After the relatively linear increase, all homogeneous cores present a slower increase, which indicates that the process of salt precipitation is close to being completed. In general, the higher-permeability core (Bentheimer) occurs salt precipitation earlier than the lower-permeability cores (Berea and Fontainebleau). At the end of salt precipitation, the pressures for the three homogeneous cores reach the highest values and remain stable. Compared to homogeneous cores, the heterogeneous core displays more complex pressure responses and takes a longer time to appear salt precipitation until 0.8 normalized injection time, which reflects the water relocation due to the capillary cross-flow and permeability contrast effects and the delayed response for the salt precipitation. Due to the pressure transducers being directly connected to the tubing, the pressure reflects inside the entire system. Therefore, we do not consider the mechanical instability from the core materials and setup that can influence the pressure response.

1.4. Impact of halite precipitation on CO_2 injectivity

To better understand the impact of halite precipitation on rock permeability, the CO_2 permeability reduction along the length of the core samples is evaluated, as shown in Fig. 13a. This figure shows the quantified permeability loss (k/k_0, equivalent to CO_2 injectivity) in different sections of the cores, near section 1 (0–21 mm), section 2 (21–65 mm), and across the entire core length.

The most significant permeability loss occurs in Section 1 (0–21 mm) due to capillary-driven backflow, where brine is drawn toward the drying front and results in pore-blocking by halite deposition near the injection point. This accelerates permeability decline, particularly in high-permeability cores like Bentheimer (2164 mD in section 1), which experience nearly complete permeability loss (∼99 %), while lower-permeability cores such as Berea (161 mD in section 1) retain some conductivity (∼83 % loss). Section 1 in Fontainebleau (164 mD) presents–89 % permeability loss. This trend provides evidence for the hypothesis that halite precipitation induces larger permeability loss in higher permeability cores. In Section 2 (21–65 mm), permeability impairment varies significantly (9–90 %), depending on rock type and brine redistribution. Although high permeability does not imply stronger capillary backflow, in high-permeability and high-porosity sandstones, CO_2 can penetrate more efficiently and expose a larger internal pore volume to evaporation, which allows halite to precipitate deeper in the core and to block critical flow pathways.

One interesting finding is that Fontainebleau (187 mD) has a higher permeability in section 2 than Berea (165 mD), while the permeability loss is much less. This can be caused by the smaller porosity, where the

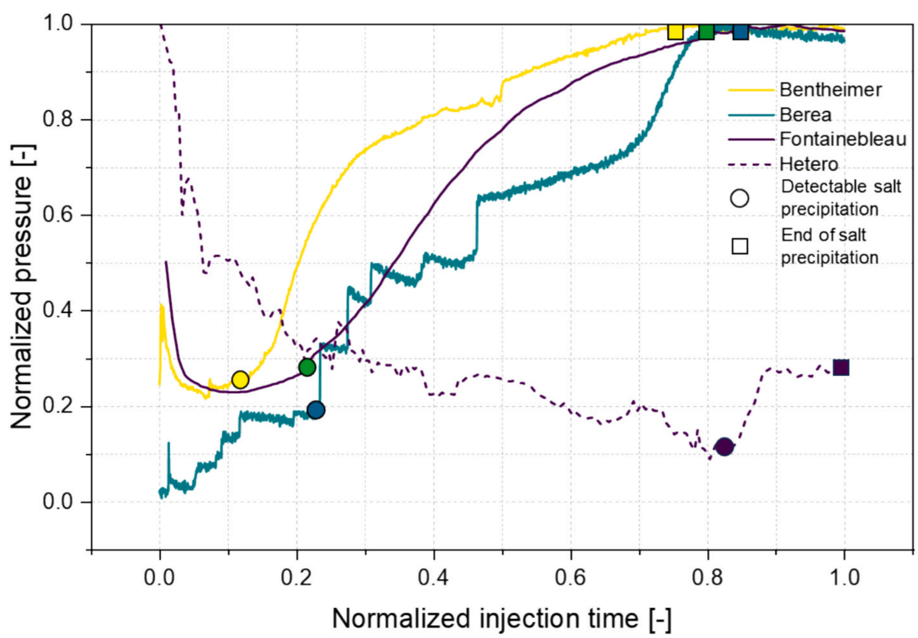

Fig. 12. Normalized pressure VS normalized injection time for four cores.

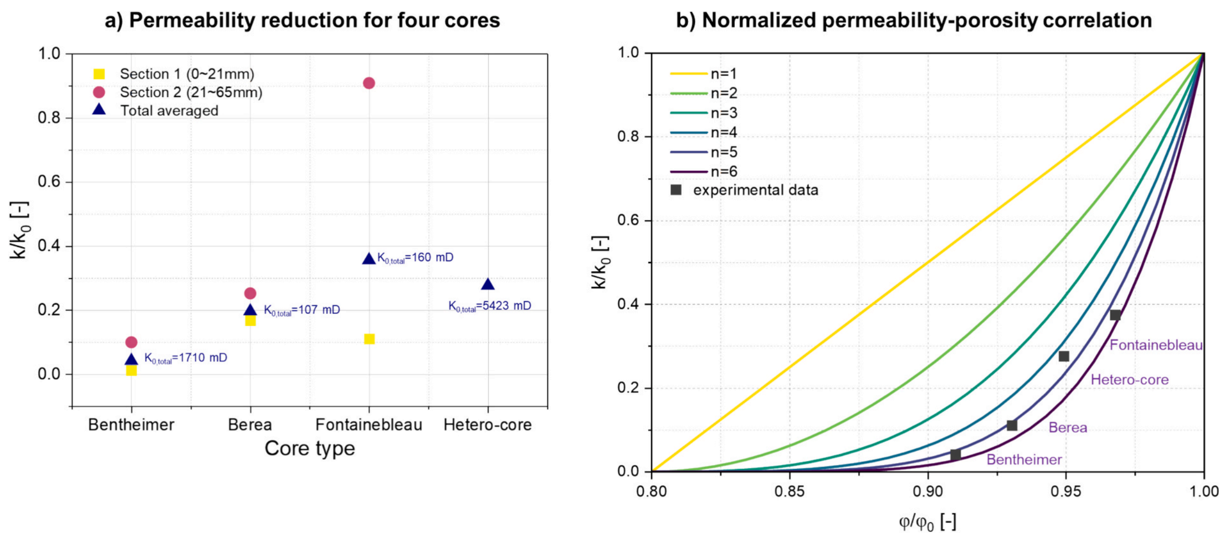

Fig. 13. Permeability reduction for four cores. (a) presents the permeability reduction in section 1 (0–21 m), section 2 (21–65 mm), and the total length of each core. (b) gives the normalized permeability-porosity correlation.

pore space is smaller and the local capillary pressure is higher. The comparison between Berea and Fontainebleau shows that porosity and capillary retention must be considered together with permeability. Although Fontainebleau has a comparable sectional permeability in part of the core, its lower porosity and stronger capillary retention promote shallower salt localization and a different permeability-loss response. Therefore, the results in Fig. 13a could be interpreted as evidence of coupled permeability-porosity-mineral heterogeneity control rather than a simple permeability trend. However, the result in the heterogeneous core shows a contradictory phenomenon, where the high permeability region does not induce a higher permeability loss. This is because most of the brine is accumulated at the top of the core surface, as shown and discussed in Section 3.3, which indicates that the stronger local heterogeneity of rock results in a different pattern of brine backflow and halite deposition.

Fig. 13b presents the normalized permeability-porosity correlation and illustrates how permeability declines as porosity decreases due to halite precipitation. The porosity–permeability relationship is described in [28] as:

$$\frac{k}{k_0} = \left(\frac{\varphi - \varphi_c}{\varphi_0 - \varphi_c}\right)^n \tag{1}$$

where k_0 is the initial permeability of the core, φ, φ_0, φ_c are the final porosity, the initial porosity and the critical porosity below which rock permeability drops to zero, and n is a fitting exponent. In sandstones, the value of n is $1 \leq n \leq 6$ and the critical porosity has a range of 0.8 φ_0 to 0.9 φ_0 [35]. In this study, we take the value $\varphi_c = 0.8\varphi_0$. From the measurement in experiments, the result is consistent with the above relationship at the exponent $n = 5$. The Verma-Pruess relationship is used here only as an empirical reference for normalized permeability-porosity trends, not as a mechanistic predictor of localized salt clogging. Because halite precipitation is strongly localized near the inlet and at permeability interfaces, the REV assumption behind a bulk porosity–permeability correlation is only partly satisfied. The mismatch between localized damage and bulk porosity is now emphasized as a limitation of the correlation. These observations are consistent with previous numerical and experimental studies showing that dry CO_2 injection can generate a local evaporation front, increase brine salinity, and induce halite precipitation near the injection region [15,20,23]. The localization of salt near the inlet also agrees with core-scale and field observations of injectivity impairment [4,26]. Compared with earlier homogeneous-core experiments, the present CT data further show that radial permeability contrast can redirect brine toward interfaces and surfaces, producing salt patterns that cannot be explained by a uniform-core capillary-backflow mechanism alone.

4. Proposed mechanism for halite precipitation in rock cores

Fig. 14 illustrates the halite precipitation mechanisms due to CO_2 injection and dry-out in homogeneous and heterogeneous cores. During CO_2 injection into a porous rock, the displacing CO_2 phase pushes brine out of the pore space, and the core retains residual brine (e.g., $S_w \approx 50$ %). When the injection rate stabilizes, the brine distribution reaches a quasi-equilibrium state. As water progressively evaporates into the CO_2 phase, brine reaches halite solubility limit and halite crystallizes. Accumulated halite crystals are formed in the porous structure and significantly reduce rock porosity, which results in higher capillary forces. The difference between this halite-induced capillary force and the intrinsic capillary pressure of rock drives capillary-driven brine backflow, where brine migrates back toward the CO_2 injection zone. The extent of this backflow is determined by the magnitude of the capillary pressure gradient. The brine movement depends on the local force balance between the viscosity force and the capillary force [15]. Besides, the inherent hydrophilicity of halite crystals absorbs the brine through brine films along the rock grains, which enhances the brine gathering to form brine clusters [33].

In high-permeability cores (e.g., 4000 mD), lower intrinsic capillary pressure results in a shorter distance of brine backflow and deeper halite precipitation within the rock matrix. Conversely, in low-permeability cores (e.g., 160 mD), a stronger difference in capillary pressures promote more extensive brine migration, leading to shallower halite deposition closer to the injection point. Additionally, the gap between the core and the injection port contributes to the halite distribution. The drier CO_2 phase near the injection point results in the initial halite precipitation near the injection location. This enhances further brine redistribution and localized halite accumulation at the injection interface. The accumulated halite within the porous medium reduces porosity and further enhances local capillary pressure in pores. As halite deposition continues and pore connectivity diminishes, CO_2 permeability declines significantly and a substantial reduction in injection efficiency is observed.

In heterogeneous systems, such as a low-permeability core (160 mD) encapsulated by a high-permeability outer layer (4000 mD), capillary pressure contrasts between the two layers significantly influence brine relocation and halite precipitation patterns. After CO_2 injection, the low-

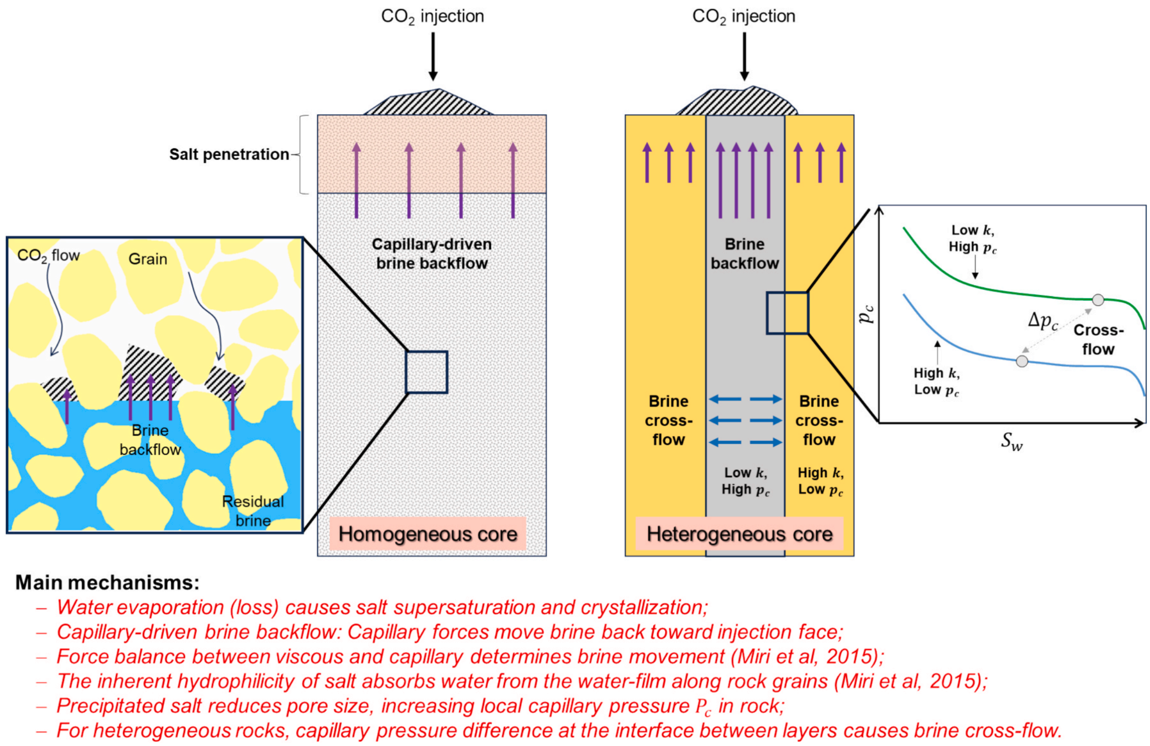

Fig. 14. Schematic of capillary-driven brine flow. The left part is the illustration for the scenario of a homogeneous core and the right part is for the heterogeneous core. The third and fourth point in the red text can be found in the literature [15]. (For interpretation of the references to colour in this figure legend, the reader is referred to the web version of this article.)

permeability core retains a higher water saturation with stronger capillary forces, while the high-permeability layer maintains a lower capillary forces, which is shown as the two grey circles on the capillary curves in the right part of Fig. 14. With the process of salt precipitation, the capillary pressure differential between the two layers (grey-dashed arrow) drives capillary cross-flow from the low to the high-permeability layer. The surface of the two layers has halite precipitation, as the raw image of the inlet cap shows in Fig. 9a. As halite precipitates close to the injection point and on the surface of the core, the low-permeability region accumulates more halite and forms a halite boundary between two layers. Therefore, the combined contributions of capillary-driven brine backflow and crossflow induced by the strong capillary forces result in an ultimate halite concentration at the surface of the heterogeneous core, which is more pronounced than it is in homogenous cores.

5. Conclusion

This study presents a systematic investigation into the effects of reservoir rock permeability and heterogeneity on halite precipitation and CO_2 injectivity impairment using core-flooding experiments coupled with real-time CT imaging. The results demonstrate that the spatial distribution of halite precipitation is heavily influenced by rock permeability variations. In homogeneous cores, halite predominantly accumulates near the injection point due to capillary-driven backflow, forming a concentrated blockage that significantly reduces permeability. In contrast, heterogeneous cores exhibit more complex halite deposition patterns, with brine migration occurring across permeability interfaces, which leads to the distributed halite accumulation rather than localized pore clogging. The heterogeneous core represents a simplified near-wellbore radial permeability contrast system. The results are therefore most applicable to local composite structures, fracture-adjacent regions, and permeability contrast zones near injection points. Extrapolation to reservoir-scale heterogeneity is not reproduced in the laboratory core. The permeability reduction in homogeneous cores follows a more predictable trend, whereas heterogeneous formations exhibit irregular injectivity decline due to permeability contrasts and capillary cross-flow effects. These findings highlight the necessity of incorporating reservoir heterogeneity into predictive models for CO_2 storage operations.

Moreover, the study underscores the role of permeability-dependent capillary pressure gradients in controlling halite precipitation dynamics. The experimental observations in the homogeneous cores confirm that higher-permeability cores experience more severe injectivity reduction due to larger pore spaces facilitating brine redistribution. This enhances the localized halite supersaturation and crystal growth. Conversely, in low-permeability zones, stronger capillary forces lead to shallower halite deposition closer to the injection point. In addition, the lower porosity in the rock leads to a lower halite penetration and permeability reduction, which reflects the fact that the porosity is also playing an important role in the halite precipitation. However, one note is that the permeability is not the only factor determining the salt precipitation. We state that the salt-induced permeability loss depends on the interaction between initial rock properties, pore connectivity, capillary redistribution, and mineral heterogeneity. We therefore avoid claiming a universal monotonic relationship between initial permeability and injectivity impairment. These insights suggest that optimizing CO_2 injection strategies, such as flow rate regulation and careful selection of the injection reservoir with well-known permeability, porosity and rock properties, may help mitigate halite precipitation risks. Future research will focus on integrating experimental data into numerical models to refine predictions of injectivity decline under varying reservoir conditions, thereby contributing to the long-term effectiveness of geological CO_2 sequestration.

CRediT authorship contribution statement

Lifei Yan: Writing – original draft, Visualization, Software, Methodology, Formal analysis, Data curation. **Rens Florian van der**

Vleuten: . **Saba Najjari Hagh:** Methodology, Formal analysis, Data curation. **Sian Jones:** Formal analysis, Data curation. **Mahnaz Aghajanloo:** Data curation. **Manon Arianne Renée Schellart:** Data curation. **Diederik Boersma:** Writing – review & editing, Supervision. **Denis Voskov:** Writing – review & editing, Supervision, Project administration. **Rouhi Farajzadeh:** Writing – review & editing, Supervision, Project administration.

Declaration of competing interest

The authors declare that they have no known competing financial interests or personal relationships that could have appeared to influence the work reported in this paper.

Acknowledgement

The authors thank Shell Global Solutions International B.V. for their permission to publish this paper. Jeroen Snippe is acknowledged for a detailed review of the draft manuscript. The authors also note that the content does not constitute operational guidance. The views expressed in this publication are those of the authors and do not necessarily reflect the views of Shell or its affiliates.

Appendix A. Supplementary data

Supplementary data to this article can be found online at https://doi.org/10.1016/j.ecmx.2026.102070.

Data availability

Data will be made available on request.

References

[1] Ajayi T, Gomes JS, Bera A. A review of CO_2 storage in geological formations emphasizing modeling, monitoring and capacity estimation approaches. Pet Sci 2019;16:1028–63.
[2] Al-Menhali A, Krevor S. Effective wettability measurements of CO_2-brine-sandstone system at different reservoir conditions. Energy Procedia 2014;63:5420–6.
[3] Al Saadi F, Wolf K, Kruijsdijk C. Characterization of Fontainebleau sandstone: Quartz overgrowth and its impact on pore-throat framework. J Pet Environ Biotechnol 2017;8:1–12.
[4] Bacci G, Korre A, Durucan S. Experimental investigation into salt precipitation during CO_2 injection in saline aquifers. Energy Procedia 2011;4:4450–6.
[5] Boon M, Hajibeygi H. Experimental characterization of H_2/water multiphase flow in heterogeneous sandstone rock at the core scale relevant for underground hydrogen storage (UHS). Sci Rep 2022;12:14604.
[6] Cui G, Hu Z, Ning F, Jiang S, Wang R. A review of salt precipitation during CO_2 injection into saline aquifers and its potential impact on carbon sequestration projects in China. Fuel 2023;334:126615.
[7] Cui G, Ren S, Rui Z, Ezekiel J, Zhang L, Wang H. The influence of complicated fluid-rock interactions on the geothermal exploitation in the CO_2 plume geothermal system. Appl Energy 2018;227:49–63.
[8] Cui G, Wang Y, Rui Z, Chen B, Ren S, Zhang L. Assessing the combined influence of fluid-rock interactions on reservoir properties and injectivity during CO_2 storage in saline aquifers. Energy 2018;155:281–96.
[9] Edem, D., Abba, M., Nourian, A., Babaie, M., Naeem, Z., 2020. Experimental investigation of the extent of the impact of Halite precipitation on CO_2 injection in deep saline aquifers, SPE Europec featured at EAGE Conference and Exhibition? SPE, p. D011S002R003.
[10] Gaurina-Međimurec N, Novak-Mavar K, Majić M. Carbon capture and storage (CCS): Technology, projects and monitoring review. Min Geol Petrol Eng Bull 2018;33:1–15.
[11] Gibson-Poole CM, Taplin M, Bouffin N, Duffy L, Sutherland F, Cabral A, et al. Site characterization of the endurance CO_2 store, southern north sea, uk. Geoenergy 2024;2. geoenergy2024–2012.
[12] He D, Jiang P, Xu R. Pore-scale experimental investigation of the effect of supercritical CO_2 injection rate and surface wettability on salt precipitation. Environ Sci Technol 2019;53:14744–51.
[13] Mascle M, Rosenberg E, Roboele B, Kowalewski E, Youssef S. Investigation of waterflood front digitations during immiscible displacements in porous media. Oil Gas Sci Technol Rev d'IFP Energies Nouvelles 2021;76:71.
[14] Miri R, Hellevang H. Salt precipitation during CO_2 storage—A review. Int J Greenhouse Gas Control 2016;51:136–47.
[15] Miri R, van Noort R, Aagaard P, Hellevang H. New insights on the physics of salt precipitation during injection of CO_2 into saline aquifers. Int J Greenhouse Gas Control 2015;43:10–21.
[16] Mukherji, A., 2023. Climate change 2023 synthesis report.
[17] Muller N, Qi R, Mackie E, Pruess K, Blunt MJ. CO_2 injection impairment due to halite precipitation. Energy Procedia 2009;1:3507–14.
[18] Ott H, Andrew M, Snippe J, Blunt MJ. Microscale solute transport and precipitation in complex rock during drying. Geophys Res Lett 2014;41:8369–76.
[19] Ott H, de Kloe K, Marcelis F, Makurat A. Injection of supercritical CO_2 in brine saturated sandstone: pattern formation during salt precipitation. Energy Procedia 2011;4:4425–32.
[20] Ott H, Roels S, De Kloe K. Salt precipitation due to supercritical gas injection: I. Capillary-driven flow in unimodal sandstone. Int J Greenhouse Gas Control 2015;43:247–55.
[21] Pereira G. Fluid flow, relative permeabilities and capillary pressure curves through heterogeneous porous media. App Math Model 2019;75:481–93.
[22] Plug W-J, Bruining J. Capillary pressure for the sand–CO_2–water system under various pressure conditions. Application to CO_2 sequestration. Adv Water Resour 2007;30:2339–53.
[23] Pruess, K., Müller, N., 2009. Formation dry-out from CO_2 injection into saline aquifers: 1. Effects of solids precipitation and their mitigation. Water Resources Research 45.
[24] Rasool MH, Ahmad M, Ayoub M. Selecting geological formations for CO_2 storage: a comparative rating system. Sustainability 2023;15:6599.
[25] Roels SM, El Chatib N, Nicolaides C, Zitha PL. Capillary-driven transport of dissolved salt to the drying zone during CO_2 injection in homogeneous and layered porous media. Transp Porous Media 2016;111:411–24.
[26] Smith N, Boone P, Oguntimehin A, van Essen G, Guo R, Reynolds MA, et al. Quest CCS facility: halite damage and injectivity remediation in CO_2 injection wells. Int J Greenhouse Gas Control 2022;119:103718.
[27] Torskaya T, Shabro V, Torres-Verdín C, Salazar-Tio R, Revil A. Grain shape effects on permeability, formation factor, and capillary pressure from pore-scale modeling. Transp Porous Media 2014;102:71–90.
[28] Verma A, Pruess K. Thermohydrological conditions and silica redistribution near high-level nuclear wastes emplaced in saturated geological formations. J Geophys Res Solid Earth 1988;93:1159–73.
[29] Wang B, Wang X, Liang Q, Chang Y, Ma R, Lin Z, et al. Investigation of pore-scale evaporative drying, salt precipitation and crystallization migration in CO_2 injection process by a Lab-On-A-chip system. SPE Can Energy Technol Conf SPE 2024. D011S005R002.
[30] Wang Y, Liu Y. Impact of capillary pressure on permeability impairment during CO_2 injection into deep saline aquifers. J Cent South Univ 2013;20:2293–8.
[31] Wright, I., Ringrose, P., Mathieson, A., Eiken, O., 2009. An overview of active large-scale CO_2 storage projects, SPE International Conference on CO_2 Capture, Storage, and Utilization. SPE, pp. SPE–127096–MS.
[32] Würdemann, H., Möller, F., Kühn, M., Heidug, W., Christensen, N.P., Borm, G., Schilling, F.R., Group, C.S., 2010. CO_2SINK—From site characterisation and risk assessment to monitoring and verification: One year of operational experience with the field laboratory for CO_2 storage at Ketzin, Germany. International Journal of Greenhouse Gas Control 4, 938–951.
[33] Yan L, Niftaliyev R, Voskov D, Farajzadeh R. Dynamics of salt precipitation at pore scale during CO_2 subsurface storage in saline aquifer. J Colloid Interface Sci 2025;678:419–30.
[34] Yusof MAM, Neuyam YAS, Ibrahim MA, Saaid IM, Idris AK, Mohamed MA. Experimental study of CO_2 injectivity impairment in sandstone due to salt precipitation and fines migration. J Pet Explor Prod Technol 2022;12:2191–202.
[35] Zhang S, Liu H-H. Porosity–permeability relationships in modeling salt precipitation during CO_2 sequestration: Review of conceptual models and implementation in numerical simulations. Int J Greenhouse Gas Control 2016;52:24–31.